ACS APPLIED NANO MATERIALS

www.acsanm.org Article

Sprayed Nanometer-Thick Hard-Magnetic Coatings with Strong Perpendicular Anisotropy for Data Storage Applications

Andrei Chumakov,* Calvin J. Brett, Korneliya Gordeyeva, Dirk Menzel, Lewis O. O. Akinsinde, Marc Gensch, Matthias Schwartzkopf, Wei Cao, Shanshan Yin, Manuel A. Reus, Michael A. Rübhausen, Peter Müller-Buschbaum, L. Daniel Söderberg, and Stephan V. Roth*

Cite This: *ACS Appl. Nano Mater.* 2022, 5, 8741−8754 Read Online

ACCESS | Metrics & More | Article Recommendations | Supporting Information

ABSTRACT: The rapid growth of digital information in the world necessitates a big leap in improving the existing technologies for magnetic recording. For the best modern perpendicular recording, the highest coercivity materials with minimal volume are required. We present a study of a facile technology for establishing mono- and multilayer surfaces from various single-domain flat magnetic nanoparticles that exhibit a strong perpendicular-oriented magnetic moment on solid and flexible substrates. Surfactant-free, hard ferromagnetic, and single-domain anisotropic strontium hexaferrite $SrFe_{12}O_{19}$ nanoparticles with a perpendicular magnetic moment orientation and two different aspect ratios are self-ordered into magnetic thin nanofilms, exploiting the templating effect of cellulose nanofibrils and magnetic fields. Uniform magnetic coatings obtained by the scalable layer-by-layer spray deposition from a monolayer coverage up to thicknesses of a few tens of nanometers show a preferred in-plane orientation of the hard-magnetic nanoparticles. High coercivities of the films of up to 5 kOe and a high perpendicular anisotropy of $M_{r\perp}/M_s > 80\%$ are found. The application of the magnetic field during film deposition ensures additional improvement in perpendicular magnetic anisotropy and the appearance of residual magnetization in the film of up to $0.6M_s$. For low-aspect-ratio nanoparticles stacked in periodic planar structures, the signs of the photonic band gap are revealed. The ability to create scalable, thin magnetic structures based on nanosized particles/building blocks opens great opportunities for their application in a wide variety of optoelectronic and magnetic storage devices.

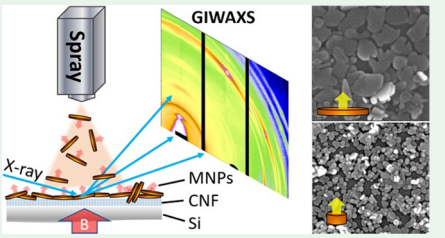

KEYWORDS: *strontium hexaferrite, magnetic nanoparticles, GIWAXS, GISAXS, ferrofluid, self-assembly, spray*

INTRODUCTION

Flexible ultrathin hard-magnetic coatings are heavily exploited in numerous fields, including magnetic storage, authenticity, counterfeit marks, Kerr rotators, and high-accuracy encoders.[1−7] Being a pioneering technology, magnetic tape recording also gained a new lease of life with the recent IBM announcement of a new record in the recording areal density exceeding 300 Gb/in.^{2} and allowing more than a half-petabyte capacity of a single-tape cartridge using magnetic nanoparticles (MNPs).[8] Tapes are still reliably and widely used for data backup and are considered the favored and cheapest solution for future cloud storage. Magnetic tapes traditionally rely upon perpendicular recording technology. This technology achieves higher storage densities by aligning the poles of the magnetic elements (MNPs or magnetic volume). The poles act as bits, perpendicular to the surface of the hard disk, and can provide more than 3 times the storage density compared to a longitudinal recording. The data storage medium evolved with the years such that coarse grain magnetic ferrites to fine particulate flat strontium hexaferrite nanolayers showing high perpendicular magnetic field anisotropy are obtained.[8] High magnetocrystalline anisotropy and texturing of fine particles are therefore essential tools to reach the medium's high coercivity and sufficient data storage stability. Strontium hexaferrite- and $SrFe_{12}O_{19}$-based substitutional phases are regarded as promising data storage media providing maximum magnetic moment with the highest magnetocrystalline and crystalline anisotropy to induce both the oriented growth of grains and the stable moment alignment at minimum nanocrystal volume.[9−11] Very similar tasks arise in the development of hard-magnetic insulator layers for flexible spintronic devices.[12−16]

Despite being the cheapest mass-market solution for years, the magnetic coating technology still requires further progress in optimizing the production pathways while retaining the high quality of the resulting medium.[17−22] To date, most of the efforts in technological improvement concern physical vapor deposition (PVD) of textured hexaferrite phases.[9,23,24]

Received: December 30, 2021
Accepted: February 25, 2022
Published: June 17, 2022

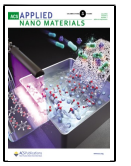

However, with PVD, crystal growth kinetics are limited by the deposition rate[25] and post-treatment duration, slowing the tape spooling conveyor during processing. Sputter deposition provides in-plane texturing in the absence of any crystallographic relation of newly formed phases to the underlying substrates.[26,27] It diminishes an effective coercive force of the magnetic layer and results in spontaneous remagnetization of the adjacent grains.[28]

Self-organization approaches highlight an alternative pathway to aligned, fine particulate films.[29] With predefined platelet-shape anisotropy, the nanoparticles will tend to align on the flat surface, more likely providing a homogeneous coating with the flat orientation of nanoplatelets. Such a nanocoating is readily formed on liquid−solid interfaces with spray-[30,31] or spin-casting[32,33] techniques or can be transferred to a solid substrate from a liquid−air interface using the Langmuir−Blodgett approach.[34] From a theoretical point of view, forming a thin monolayer of highly anisotropic particles with ultimate magnetocrystalline anisotropy is of major importance. With an actual magnetic recording track width in tape prototypes of ∼50 nm,[8] the particle size in the medium should not exceed this value.

Platelet-shaped $SrFe_{12}O_{19}$-nanoparticles of such sizes are readily available in a colloidal form with industrial-scale quantities using the glass crystallization technique.[11,35,36] The nanoplatelets' average sizes, anisotropy parameters, and magnetic properties are well controlled with glass composition and treatment temperatures.[37,38] After the glass dissolution, these nanoparticles can be successfully transformed into surfactant-free colloids stabilized by an electrical charge.[38] Contrary to the traditional magnetic liquids, such colloids contain fine single-domain ferromagnetic nanoplatelets with a rigidly fixed magnetic moment that's stabilized with a strong magnetocrystalline anisotropy of $SrFe_{12}O_{19}$.[39] In contrast to the properties of the fixed individual particle, the magnetic properties of a ferromagnetic colloid exhibit a minimal magnitude of the coercive force of the order of several Oersted due to the ability of magnetic particles to freely change their orientation in a liquid medium by the action of a minimal external magnetic field[38,40,41] and allow for facile manipulation during the drying process.

The scalable spray-drying deposition method can be easily used for a new and facile approach to creating the needed thin and flexible magnetic layers. Recently, spray-deposited hybrid polymer films of asymmetric diblock copolymer polystyrene-*block*-poly(methyl methacrylate) (PS-*b*-PMMA) and magnetic nanoplatelets were suggested[42,43] as being applicable as absorbers at microwave and mm-wave frequencies.[44,45] However, both the magnetic moment and anisotropy of strontium hexaferrite nanoplatelets are expected to significantly affect the final magnetic properties of the casted arrays and the size of magnetically correlated regions. Moreover, with the wide variability in the packing options of nanoplatelets in the self-assembled media, it is necessary to understand the impact of the main parameters on the magnetic arrangement. Thus, in the present study, we focused on revealing the role of the anisotropy of hard-magnetic nanoplatelets and their ordering in the arrays on the magnetic characteristics of spray-deposited nanopatterned films, applying external magnetic fields and cellulose nanofibrils as structural templates to guide the self-organization.[46,47]

EXPERIMENTAL SECTION

Materials and Sample Preparation. Strontium hexaferrite magnetic MNPs and the corresponding stable aqueous colloidal solution were prepared using the glass−ceramic dissolution technique developed in the previous literature.[38] Two types of particles, first high and then low diameter-to-thickness ratios, were prepared. The first one was made using 4 Na_2O·9 SrO·5.5 Fe_2O_3·4.5 Al_2O_3·4 B_2O_3 glass composition and thermal treatment at T = 700 °C for 2 h. These particles were adopted and characterized in previous research.[40] The prepared colloidal solutions using this current composition and temperature are referred to as NAL in the present study. The second step was prepared using a different composition: 14 SrO·6 Fe_2O_3·6 B_2O_3 with a similar 2 h thermal treatment at T = 680 °C. These prepared colloidal solutions using current composition and temperature are referred to as SHF in the present study. The glassy borate matrix was dissolved in 3% hydrochloric acid. The magnetically active precipitate was separated by decantation on a magnet and dispersed in distilled water by sonication to form stable dispersions of hexaferrite nanoparticles.

The prepared colloidal solutions were centrifuged for 120 min and then held on the magnet until concentrated phase formation for more accessible storage and further processing.[41] The concentrated phase was diluted to restore the initial colloid state before spray deposition. Thermogravimetric analysis (TGA) was performed to determine the actual sample concentration. In addition, transmission electron microscopy (TEM) imaging allowed the determination of actual particle size distributions.

Hexaferrite deposition on silicon wafers was performed according to the technique previously reported.[30,48,49] The silicon wafer from the Si-Mat company with a thickness of 675 ± 25 μm, a resistivity of 1−30 Ω·cm, type-oriented P/boron ⟨100⟩, single-side-polished was used. Silicon substrates were precleaned by keeping the plates in a mixture of concentrated sulfuric acid and hydrogen peroxide for 15 min at 80 °C.[48]

The nanocellulose coating as a second kind of substrate was also produced by spray deposition of cellulose nanofibrils (CNFs) in water. Subsequently, the deposition of a magnetic colloid was carried out on the surface of a preformed cellulose film. The surface charge density of CNF was 1360 μmol/g.[2,48] The resulting film possessed a thickness of ∼160 ± 2.5 nm. For hexaferrite coating, 1 or 10 spray cycles were used to form thin or thick films of magnetic nanoparticles, respectively. Spray coating as a very good scalable technique was fulfilled by a spray-coating device (Compact JAUD555000, Spray Systems, Germany) at a nitrogen gas pressure of 1 bar, a nozzle−substrate distance of 200 mm, and a room temperature of 22 °C. The Si wafers were placed onto a nonmagnetic heating plate of 120 °C.[48,50] The temperature and other process parameters of the spray device used have been well tested to obtain a homogeneous distribution of the spray liquid over the surface during drying and to avoid coagulation of the dried drops or the formation of the "coffee ring" effect.[50] A homogeneity of the nanofilms, prepared by this technique and parameters, was published in ref 48 and used as a standard protocol. The real drying time of the liquid colloidal film is around a second, which is more than enough for the orientation and stacking of particles. In addition, magnetic particles are free to rotate in the liquid phase, which is suppressed due to the fast drying. The consequence of this is a very low coercivity of liquid colloid on the order of several Oersted and fast particle rotation under the action of an external alternating magnetic field of up to 100 Hz.[38,40] Thus, considering completely different direct or indirect factors, we believe that the drying time of the colloid of a second is more than enough for the correct orientation of the particles according to the surface topography and local magnetic fields of the already applied layer of the magnetic particles. A permanent ferrite magnet with a 100 mm diameter, a 15 mm thickness, and a magnetic field of B = 0.1 T, oriented perpendicular to the substrate plane, was placed onto this heater. The surface temperature was controlled by a thermal sensor. CNF and water-based magnetic colloids were placed into a siphon plastic container connected to the spray nozzle. CNF thin films were

https://doi.org/10.1021/acsanm.1c04568
ACS Appl. Nano Mater. 2022, 5, 8741−8754

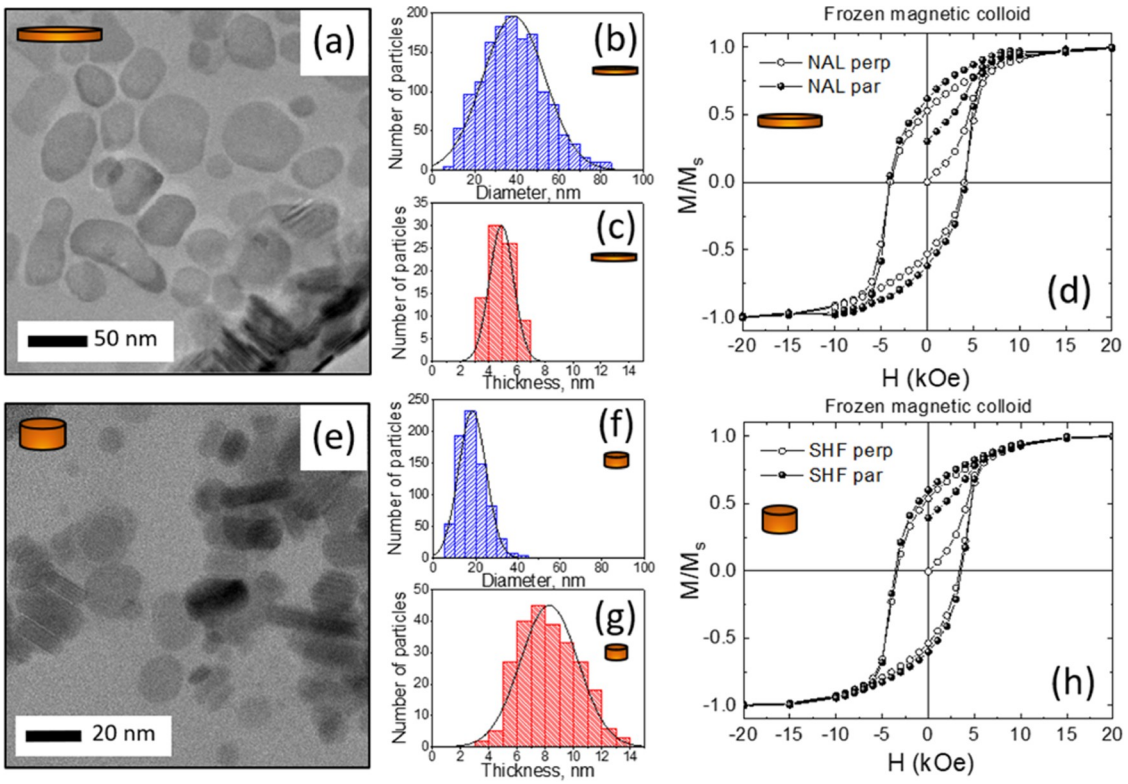

Figure 1. Transmission electron microscopy (TEM) images (a, e) and size distribution parameters (b–g) of the magnetic colloids based on nanoplatelets (denoted NAL; a–c) and nanoblock (denoted SHF; e–g). NALs have a small distribution in thickness (c) but a significant spread in lateral dimensions (b). SHF demonstrates a rather small size distribution (f) but a larger thickness distribution (g). Hysteresis loops of nanoplatelets (d) and nanoblocks (h) from the colloids frozen under the external magnetic field and measured at different orientations of the SQUID experimental field at T = 200 K demonstrate the magnetic behavior of uniformly distributed individual magnetic nanoparticles (MNPs) during the remagnetization process.

deposited using a 0.2 s spray pulse and a 10 s waiting alternated for 20 cycles.[48] One and 10 spray pulses with a time of 0.2 and 10 s waiting times were used for the magnetic colloid distribution, respectively.

The resulting coatings were analyzed by grazing incidence small- and wide-angle X-ray scattering (GISAXS, GIWAXS) and scanning electron microscopy (SEM) imaging to reveal the film microstructure. Magnetic measurements using a SQUID magnetometer allowed the determination of the magnetic properties and film thickness according to the pure hexaferrite particle properties.

Magnetic Layer-by-Layer Coating. The concentrations of the dispersions were w(SHF) = (0.063 ± 0.003) wt % and w(NAL) = (0.044 ± 0.004) wt % (Figure S2a,b) adjusted to provide a monolayer coverage of the substrates respectively a thickness corresponding to the MNPs' height with a single-spray pulse. The deposition was performed on silicon substrates covered with a native oxide layer and on ultrasmooth CNF layers with a thickness of 160 ± 3 nm, relevant for possible applications on flexible electronic devices.[48] The temperature of the substrate during the deposition was maintained at 120 °C, below the Curie temperature of $SrFe_{12}O_{19}$ (T_C = 464 °C).[51] To expose the effect of magnetically induced ordering, the field of B = 0.1 T oriented perpendicular to the substrate was also applied during the spray deposition. Thin and thick films of magnetic nanoparticles were created with the spray deposition by applying 1 and 10 spray cycles, respectively. Further, down the text, we will use the following designation for the samples: nanoplatelets (NAL) and nanoblocks (SHF) after 1 spray pulse (N1 or S1) and after 10 spray pulses (N10 or S10). An additional suffix is spraying in the presence of an external magnetic field (···H) and a prefix cellulose CNF film[48] on a silicon substrate (C···). Further information on all of the studied samples is given in the Supporting Information, Table S1.

Field-Emission Scanning Electron Microscopy (FE-SEM). SEM images of the samples after 10 spray pulses were investigated by a field-emission scanning electron microscope setup (Zeiss company) at an accelerating voltage of 1, 10, and 15 kV, located at the Center for Free-Electron Laser Science (CFEL, DESY, Hamburg, Germany). Topography of films after 1 spray pulse was studied using a field-emission scanning electron microscope (FE-SEM, Hitachi SS-4800, Japan) operated at 1 keV at the KTH Royal Institute of Technology (Stockholm, Sweden). Prior to this measurement, each sample was coated with Pt/Pd for 10 s using a Cressington sputter coater 208 HR (U.K.).

Transmission Electron Microscopy (TEM). The morphology of hexaferrite nanoplatelets was studied with a Carl Zeiss Libra 200MC (FE-SEM, Zeiss, Germany) transmission electron microscope.

Thermogravimetric Analysis (TGA). To estimate the weight fraction of the magnetic phase in dispersion, TGA was performed on TA Instruments Discovery (TGA 5500). The dispersion was heated to 105 °C at 1 °C·min^{-1} and kept at the targeted temperature for 20 min to ensure complete water evaporation. The experiment was performed in a nitrogen environment with the gas flow fixed to 10 mL·min^{-1}.

Atomic Force Microscopy (AFM). NTEGRA probe Nano-Laboratory (NT-MDT, Russia) in the semicontact mode was used for the AFM image preparation. A Cantilever ETALON HA_NC (NT-MDT, Russia) with a tip radius of 10 nm, a length of 94 μm, a width of 34 μm, and a resonant frequency of 144 kHz was utilized. The topography maps were taken with a scan size of 20 × 20, 10 × 10, 5 × 5, 3 × 3, and 1 × 1 μm^2. The program Gwyddion 2.25[52] was used for the AFM data analysis.

GISAXS/GIWAXS. For the structural investigation, the small- and wide-angle X-ray scattering in grazing incidence geometry (GISAXS/GIWAXS) experiments were performed at the Micro-and-Nanofocus X-ray scattering (MiNaXS) beamline P03 of the high-brilliance light source PETRA III at DESY, Hamburg.[53] The X-ray beam with the

https://doi.org/10.1021/acsanm.1c04568
ACS Appl. Nano Mater. 2022, 5, 8741−8754

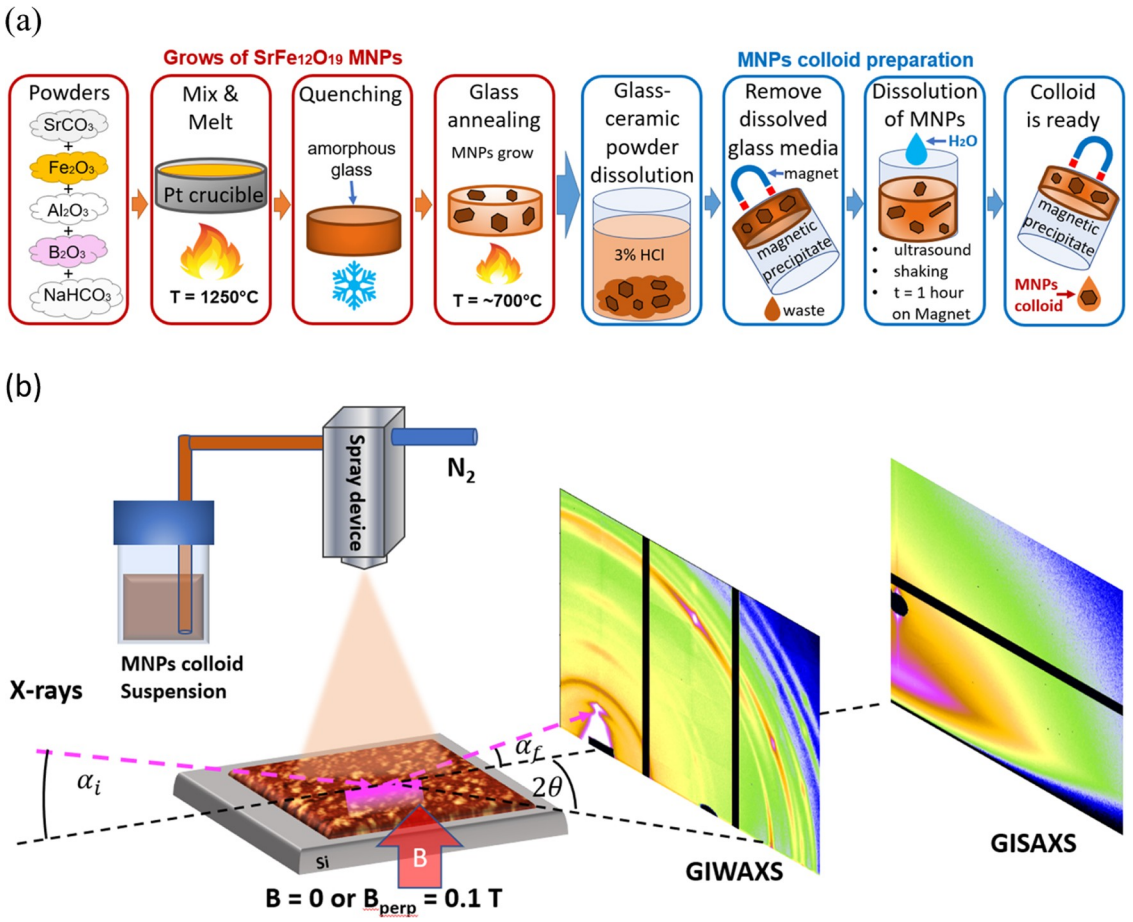

Figure 2. (a) Scheme of the nanoparticle synthesis and colloid preparation. The MNP growth part (red frames) consists of the mixture of initial powder compounds, melting one in the platinum crucible at the T = 1250 °C, next quenching to get an amorphous glass structure, and the final glass crystallization at the $T \approx 700$ °C for MNPs growing in the glass media. The MNP colloid preparation part starts from the shredding and dissolution of the glass−ceramic media with MNPs in 3% of HCl; removing the water−acid solution with the solved glass media; keeping the magnetic ceramic part by the strong permanent magnet; next adding the water, ultrasonication and shaking to dilute MNPs in the water media; and finally removing the obtained magnetic colloid, keeping the magnetic ceramic precipitate by magnet again.[38] (b) Scheme of the spray deposition process and subsequent film probed by grazing incidence wide- and small-angle X-ray scattering (GIWAXS/GISAXS). The magnetic nanoparticles are spray-deposited on the substrate without or in the presence of a perpendicular external magnetic field. The X-ray beam is indicated by the pink dashed line; $\alpha_{i,f}$ and 2θ denote the incident, the exit, and the out-of-plane angle, respectively.

energy 12.85 keV (wavelength λ = 0.965 Å, $\Delta\lambda/\lambda = 10^{-4}$) was used with a focus size of around ($V \times H$) 20 × 30 μm^2 at the sample position. The sample-to-detector distance (SDD) for GISAXS was 4340 mm and for GIWAXS 213.5 mm. The incident angle was α_i = 0.4°. Two Pilatus 300k detectors (Dectris Ltd., Switzerland), a pixel size of 172 × 172 μm^2 and an image dimension of 487 × 619 pixels used for both GISAXS and GIWAXS experiments. Ex situ GISAXS and GIWAXS measurements were carried out alternately.

SQUID Magnetometry. DC magnetic measurements were performed by the SQUID (Superconducting Quantum Interference Device) technique in the magnetic property measurement system (MPMS-XL7) Quantum Design magnetometer (BTU, Braunschweig, Germany). A precision Agilent4294A LCR meter with an operating frequency of 1 MHz was used. The magnetic properties of samples were investigated, with the orientation of the sample plane encompassing a size of around 5 × 5 mm^2 perpendicular to the applied magnetic field of the SQUID magnetometer. A typical magnetization curve explaining the magnetic properties is shown in Figure S15.

Optical Properties. DC magneto-optical measurements were carried out on a Perkin Elmer Lambda 950 using a self-developed cuvette holder equipped with an electromagnetic coil (B_{max} = 50 mT) universal reflectance accessory. The samples were scanned in the wavelength range from 250 to 885 nm with step 2 nm at reflection angles of 8, 20, 30, 40, 50, and 60°.

Computational Details. The magnetic behavior of hexaferrite nanoplatelets and their stacks was modeled using the NIST OOMMF 1.2b4 package.[54] The coercive force of particle in computation was adjusted by setting the saturation magnetization to 350e^3 A·m^{-1} and the magnetocrystalline anisotropy to 1.2 × 10^5 J·m^{-3}. The field step size in the coercive force determination process was set to 10 mT. Particles of the average lateral size of 40 nm and thickness 5 nm were adopted for the modeling. A vertical stack of two and three particles, as well as two particles lying flat at a small distance, were examined and compared in the calculations.

RESULTS AND DISCUSSION

Two types of colloids (NAL, SHF) with single-crystalline, single-domain $SrFe_{12}O_{19}$ particles and different possessing anisotropy parameters were utilized to deposit nanopatterned magnetic media. Their chemical and phase composition was confirmed in the previous works by conventional energy-dispersive X-ray (EDX) analysis and X-ray diffraction (XRD).[55,56] The plate-like shape of individual particles with an average diameter of ∼40 nm and a thickness of ∼5 nm (shape anisotropy ∼9) was resolved by TEM studies for

https://doi.org/10.1021/acsanm.1c04568
ACS Appl. Nano Mater. 2022, 5, 8741−8754

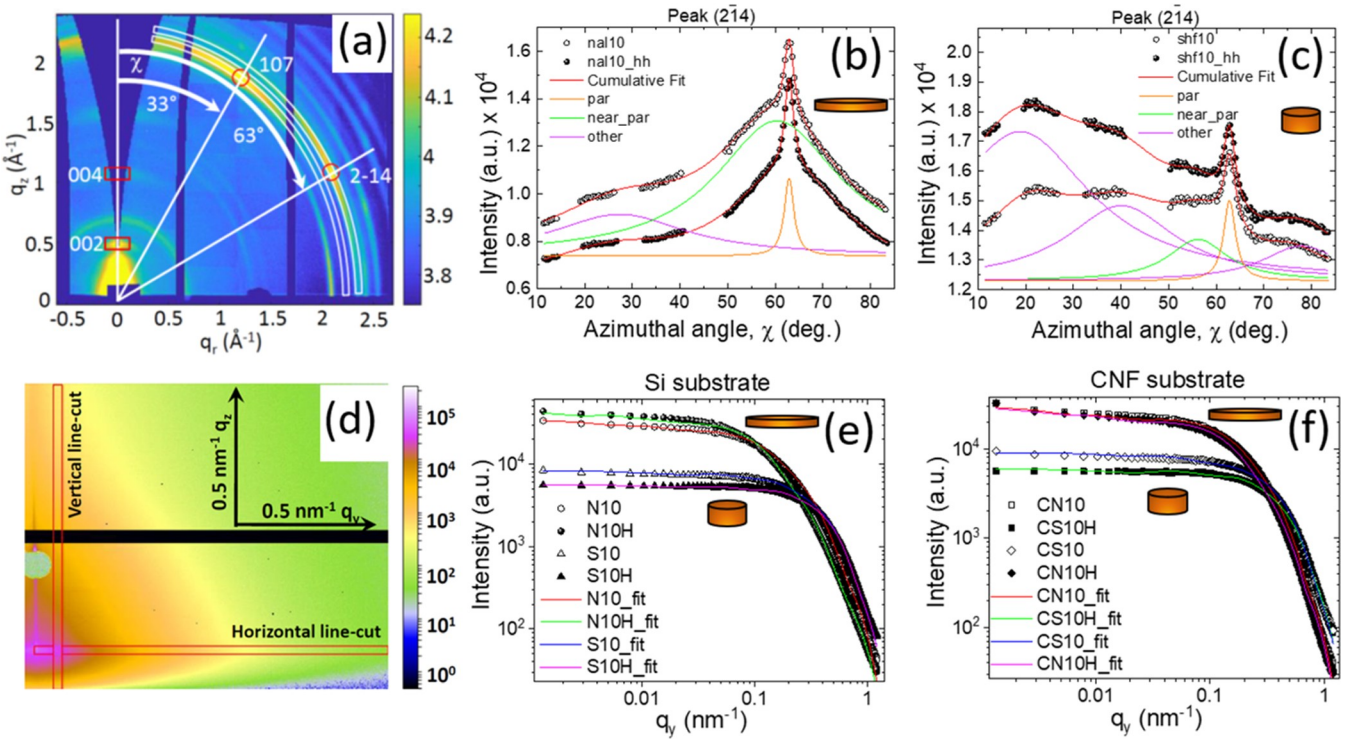

Figure 3. (a) GIWAXS data (q_z, q_r map) for NAL after 10 spray cycles. White circular arcs demonstrate the analyzed two azimuthal intensity distributions along the most intensive Bragg peaks (2−14) and (107), indicated by red circles. χ = 0° corresponds to the vertical axis (q_z), counterclockwise. (b, c) Azimuthal intensity distribution of the peak (2−14) for the nanoplatelets NAL are shown in panel (b) and for the nanoblocks SHF in panel (c) after spraying on the silicon substrate (Si) with and without the magnetic field. The azimuthal intensity distributions were fitted by the sum of Lorentz profiles (green curves); for clarity, only the Lorentzian curve contribution to the upper curves—N10 in panel (b) and S10H in panel (c)—are shown. Red curves show the cumulative fit. The large shape anisotropy of nanoplates NAL leads to the preferential orientation of particles parallel to the substrate with a small angular distribution (c). Particles SHF with a slight shape anisotropy are more susceptible to an isotropic angular distribution of particles. (d) Horizontal and vertical line-cut regions in the 2D GISAXS data of the sample NAL10 on the Si substrate. Horizontal line-cuts of the 2D GISAXS data of the nanoplatelets NAL (e) and nanoblocks SHF (f) after 10 spray pulses on the CNF film. Lines show the resulting fits according to the EIAC model, described in the text.

nanoplatelets, designated NAL (Figure 1a−c). A diameter of ∼20 nm and a thickness of 7.5 nm (shape anisotropy ∼2.5) were found for the nanoblocks designated SHF (Figure 1e−g). In the frozen MNP colloid (Figure 1d,h), a slight difference in the remagnetization curves in the parallel and perpendicular fields was observed. Freezing of the colloid was used only as an additional study to determine the magnetic signal from free-standing free particles within the colloid. Freezing was performed under the action of an external magnetic field for the unidirectional orientation of nanoparticles and subsequent SQUID measurements. A rather similar coercive force for NAL and SHF appears quite surprisingly, accounting for a rather strong difference in the probed volume of the particles (∼10^4 nm^3 in nanoplatelets vs 2 × 10^3 nm^3 in nanoblocks). These effects can be explained by the structure of platelet threads formed in the frozen dispersions.[41] This shows a good agreement with the observation in our previous study:[41] small-angle X-ray scattering (SAXS) on such dispersions shows characteristic signals for particle stacks; hence, their formation appears highly probable during freezing or solvent evaporation, as SAXS measurements of the dispersion do not show any agglomerations in the present work (Figure S18). In the case of particle stacking, the coercive force reflects both the magnetocrystalline anisotropy and collective magnetization behavior in the magnetic dipole chains.[57] The estimate of the magnetic dipole interactions between the platelets with conventional micromagnetic simulations using the NIST OOMMF 1.2b4 package[54] reveals that the magnetic characteristics of the arrays are strongly influenced by the interparticle distances. The coercive force effectively increases from 3.95 kOe for weakly interacting individual platelets at distances larger than 100 nm to >4.5 kOe for the nanoplatelet stacks with decreasing interparticle distance (see the Supporting Information, Figure S1).[41] The absence of well-defined anisotropy of the hysteresis loop in parallel and perpendicular field orientations of the nanoplatelet stacks is consistent with the single-domain structure of such concentrated magnetic liquids.

The dispersions were further utilized to spray-deposit colloidal $SrFe_{12}O_{19}$ films with the methodology described above following our earlier work.[30,48] The synthesis scheme and deposition method are shown in Figure 2. SEM images of the resulting films are provided in the Supporting Information, Figures S3 and S4, revealing a homogeneous distribution and coverage of the substrates with nanoplatelets even after a single-spray pulse; see the Supporting Information, Figure S3c,d,g,h. Most nanoparticles appear to lay parallel to the substrate plane. While SEM yields topographical and surface morphology characterization, the strong uniaxial crystallographic anisotropy of the hexaferrite phase ($P6_3/mmc$) and single-crystalline nature of the platelets require determining their orientation using diffraction methods, especially for the thicker films. Hence, GIWAXS was employed to quantify the orientations of nanoplatelets in the deposited films[58] (Figures

https://doi.org/10.1021/acsanm.1c04568
ACS Appl. Nano Mater. 2022, 5, 8741−8754

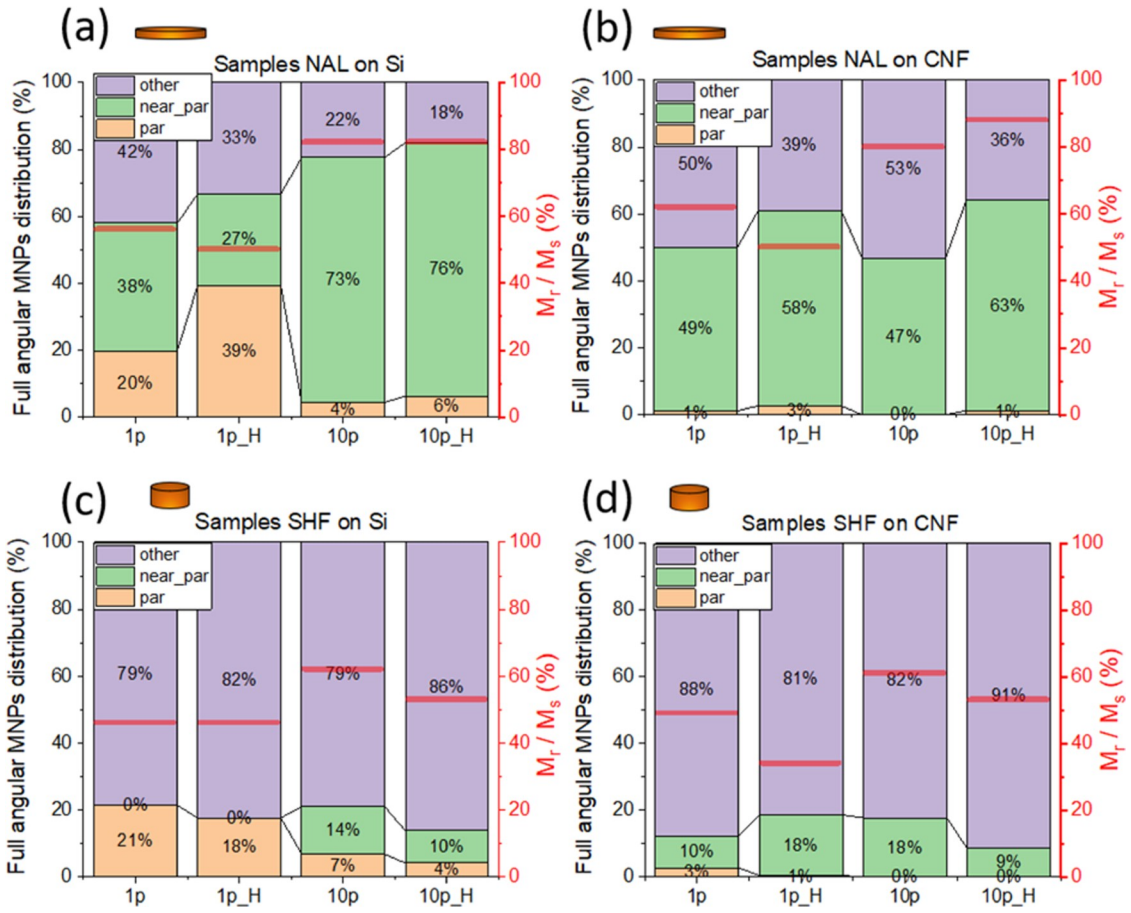

Figure 4. Column diagram of the integral peak intensity of the (2−14) reflection for NAL on Si and CNF thin film (a, b) and SHF on Si and CNF thin film (c, d). Labeling 1p and 10p correspond to the samples after 1 and 10 spray pulses, respectively, and "_H" denotes samples prepared under the influence of an external magnetic field. Diagram regions "par" correspond to the percent ratio of the integral peak intensity from the nanoparticles oriented parallel to the surface with the azimuthal (2−14) peak center around ∼62° (orange), "near_par" denotes peaks in the region 40−60°, and "other" denotes the integral intensity distribution of peaks of the (2−14) peak in the azimuthal direction for 10−40°; see description in the main text. The right ordinate M_r/M_s shows the ratio of the remanence M_r to saturation M_s in percent according to the SQUID data.

3a and S5). A typical 2D GIWAXS pattern indicates a uniaxial $SrFe_{12}O_{19}$ texture in the films, with the set of maxima corresponding to the in-plane orientation of the MNPs with the [00l] direction normal to the film surface. According to a theoretical pattern (open circles in Figure S6c), several low-index reflections can be potentially exploited to analyze the crystals' orientations with no interfering maxima at the same $\boldsymbol{q}$, such as peaks (2−14) and (107) (see the Supporting Information, Figure S6a,b), and $\boldsymbol{q}$ denotes the wavevector transfer. The angular distribution χ of the scattering intensity at a selected $|\boldsymbol{q}|$ was analyzed, suggesting the best description of nanocrystal orientation by exploiting the azimuthal intensity distribution around the (2−14) reflection at q = 2.36 Å^{-1}. Those distributions differ significantly for NAL and SHF thin films and evolve with the number of layers of hexaferrite particles (Figures 3b,c, S7 and Table S2).

The distributions of the azimuthal intensity of the peak (2−14) can be described by up to two (narrow and wide) main components located at ∼63° and up to three around 10°−40° from the surface normal. These components correspond to the platelets oriented closely parallel and near-parallel as well as strongly nonparallel orientations concerning the substrate plane, accordingly. The sharp component in Figure 3b,c (and the Supporting Information, Figure S7a,b,e,f) with a full width at half-maximum (FWHM) of ∼2° is the main contribution of MNPs deposited onto a silicon substrate. This is ascribed to the first-layer platelets ordered strictly parallel to the substrate plane. The wider component with an FWHM of 30° also appearing around the angle of ∼63° and growing with the film thickness can then be ascribed to the particles slightly misoriented from the surface plane in the above layers. The other broad components (FWHM ∼40°) located at ∼20 and ∼30° from the normal vector are suggested to correspond to the platelets, oriented significantly out of the parallel MNP orientation concerning the film plane. These components become more prominent in thicker films obtained without an external field on CNF substrates (Supporting Information, Figure S7a). In the case of nanoblocks SHF, sprayed under the magnetic field, for the thick films, it can even lead to a quasiperiodic arrangement of the threads, giving rise to the characteristic reflection in low-angle FFT pattern (see Figure S8). It results in irrigation caused by the diffracted light on the quasiperiodic structure (see also the Supporting Information, Figure S9).

There are four main parameters acting on the MNPs during the deposition: the MNP shape anisotropy-oriented magnetic moment of MNPs together with their remagnetization field, the presence of the external magnetic field, and surface charge of the substrate. The suggested analysis of the component contribution was applied to all of the samples, NAL and SHF,

https://doi.org/10.1021/acsanm.1c04568
ACS Appl. Nano Mater. 2022, 5, 8741−8754

sprayed on Si and CNF substrates with and without a magnetic field. This allows relating the above-mentioned four parameters to the MNP thin film morphology on both Si and CNF substrates for thin and thick films. The results are summarized in Figure 4. The orientations of the components around 63° of the peak (2−14) are denoted as parallel (par, FWHM ∼2°, centered around χ = 63°) and near-parallel (near-par, FWHM ∼30°, centered around χ = 63°). The components centered in all other azimuthal directions are denoted as "other" (FWHM ∼30−45°, centered around χ = 10−40°). The integral peak intensity of these components is normalized to 100% and hence depicted as relative intensities.

To start with, we estimate the orientation of nanoplatelets NAL (shape aspect ratio of ∼10) on the Si substrate (Figure 4a). Without the magnetic field, the portion of aligned particles ("par" and "near_par") for the single layer after 1 spray pulse attains around 58% in thin films and increases to 77% in thicker films. In thin films, 20% of NAL particles are parallelly oriented MNPs and just 4% for the thick film. Generally, the external magnetic field effect can be considered beneficial. It leads to a more significant portion of in-plane-oriented nanoparticles for both thin films, which contribute up to 67% to the intensity among which 39% (absolute percentage) corresponds to the integral intensity of parallelly oriented nanoplatelets. In thick films (10 spray pulses), the external magnetic fields improve the intensity attributed to the parallel orientation up to 82% including 6% attributed to in-plane-oriented particles. In the case of the CNF template, one must consider the negative surface charge of the CNF of 1360 μmol/g. Its presence will lead to the slight decrease of near-parallel intensity attributed to nanoplatelets' fraction to 50 and 47% for 1 and 10 pulses (thin/thick MNP film) without field and to 61 and 64% for 1 and 10 pulses under the external magnetic field, respectively (see Figure 4b). In general, this confirms the beneficial effect of the magnetic field.

The intensity, attributed to parallelly oriented nanoblocks SHF with an aspect ratio of ∼2.5 on the Si substrate after 1 spray pulse, shows a value of only 21 and 18% without and with the magnetic field, respectively (see Figure 4c). After 10 spray pulses, thick films will keep the proportion of the intensity related to "par" and "near_par" at 21 and 10% without and with the magnetic field, respectively. The intensity contribution of parallelly oriented MNPs decreases to 7 and 4% without and with the magnetic field, respectively. The CNF template also decreases the ratio of parallelly oriented MNPs to ∼1% with a similar integral intensity from near-parallel MNPs around 10−18% (see Figure 4d). Interestingly, the disordered portion increases strongly for thick films sprayed with the magnetic field. Special attention should be paid to the azimuthal intensity redistribution for nanoblocks after 10 spray pulses (Figures 3c and S7). The presence of an external magnetic field significantly shifts the orientation of the particles in a direction closer to χ ∼45° relative to the plane of the substrate (black circles): The peaks around χ ∼45° strongly increase in amplitude. This is in contrast to a more uniform distribution in the absence of the field (empty circles). This anisotropy of the particle distribution leads to the appearance of a quasiperiodic wave-like structure in thick films of nanoblocks under the action of the external field.

Thus, we conclude that a large shape aspect ratio for nanoplatelets (NAL) forms a layer with mainly parallelly oriented nanoplatelets, while the small aspect ratio of nanoblocks (SHF) leads to nonparallel MNP orientations. A large aspect ratio will also lead to parallel stacking of the MNPs' first layers relative to the substrate. Subsequent particle layers deposited by spray coating will lead to a blurring of this tendency. The presence of an external magnetic field will increase the tendency of planar particles to stack in parallel. The orientation of nanoblocks (SHF) in this case will shift from more parallel to the plane of the substrate (Figure 4c,d). The presence of the template with negatively charged cellulose nanofibrils should lead to the immediate trapping of positively charged MNPs, reducing their mobility during the drying process of the colloid and the disappearance of strict parallel stacking of particles in the absence of an ideally smooth surface. In addition, the stacking of particles in the drying liquid phase of the colloid will be under the significant influence of the strong magnetic moment interaction of the MNPS itself with the total local magnetic field from the magnetic moments of the already deposited particles. This shows the complexity of designing thin, functional MNP films on bio-based flexible substrates.

One may estimate the possibility of mutual influence of contributions from an oppositely charged cellulose substrate and the presence of an external magnetic field. The negatively charged CNF substrate actually prevents freer migration of positively charged MNPs together with the natural roughness in the form of individual CNF fibrils, which does not allow the first layer of particles to fit strictly parallel to the surface plane. This is visible in the GIWAXS diffraction pattern in the form of blurring of sharp diffraction peaks from particles with a strictly parallel orientation of the particles relative to the substrate (Figure S7). The presence of an external magnetic field leads to a greater tendency to parallel stacking of flat particles (nanoplatelets) (see Figures 3b and S7a,c). Particles of a more isotropic shape (nanoblocks) with a small aspect ratio begin to predominantly reorient away from the parallel arrangement (see Figures 3c and S7e,d). Thus, based on the GIWAXS data, as well as other studies, we tend to believe that the presence of an oppositely charged cellulose film and an external magnetic field creates separate contributions that do not significantly affect each other.

To investigate the agglomeration behavior of the MNPs on the Si and CNF templates, GISAXS was performed simultaneously with GIWAXS. These techniques allow an in-depth description of the nanoscale features of the self-organized structure of nanoplatelets in the agglomerates (see Figures 3d and S10). The quantitative information on the average interparticle distances is extracted from off-center scattering intensity distributions (Supporting Information, Figure S11). The increased scattering intensity in q_z-scans at $q_z \approx 0.08$ Å^{-1} for nanoblock and $q_z \approx 0.11$ Å^{-1} for nanoplatelet samples coincides with the expected period between the particles stuck together by their flat faces of ∼8.0 and ∼5.5 nm, correspondingly.

Horizontal line-cuts along q_y of the 2D GISAXS scattering pattern of the nanoblocks SHF and nanoplatelets NAL were carried out at the position of Yoneda reflection[59] at α_c = 0.14°, as shown in Figures 3e,f and S12. All scattering curves have a plateau in the region of ultrasmall angles, indicating a uniform distribution of particle agglomerates in size up to a micron. Differences between the two types of MNPs used are observed only in the region of large q. The analysis of the horizontal line-cuts of GISAXS data based on real-space morphological features was carried out using the effective interface approximation.[46,48,60] Here, one can describe the in-plane

https://doi.org/10.1021/acsanm.1c04568
ACS Appl. Nano Mater. 2022, 5, 8741−8754

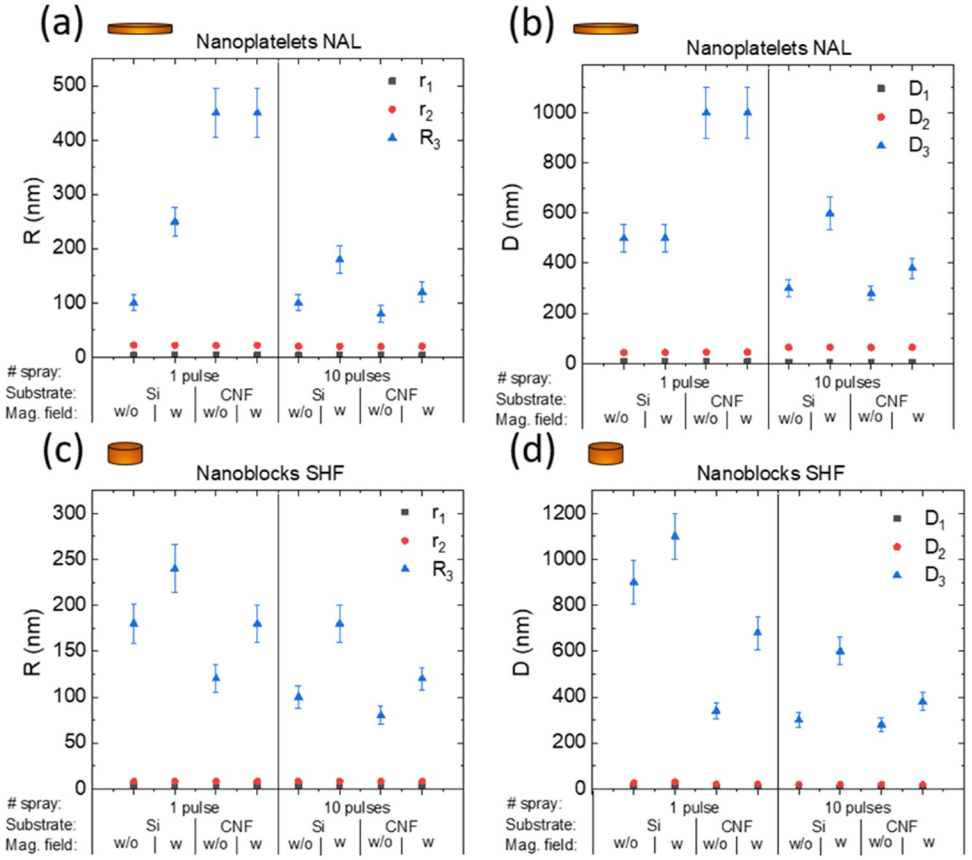

Figure 5. GISAXS fitting results according to the three effective interface approximations for cylindrical (EIAC) objects, which can describe the full in-plane radius and distance of the nanoparticle structures. r_1 (3 ± 1 nm) and D_1 (8 ± 2 nm) correspond to the thickness and distance between vertically oriented nanoparticles, r_2 and D_2 correspond to the radius of the horizontal nanoparticles and distance between the neighbor ones, and R_3 and D_3 correspond to the radius and distance of agglomerations of nanoparticles (see the model in the Supporting Information, Figure S13). r_2 parameter was 20−22 ± 3 nm for NAL and 8 ± 2 nm for SHF for 1 and 10 spray pulses. D_2 parameter was 44−46 ± 5 nm (1 pulse) and ∼65 ± 6 nm (10 pulses) for NAL and 20−26 ± 3 nm (1 pulse) and ∼18 ± 3 nm (10 pulses) for SHF particles.

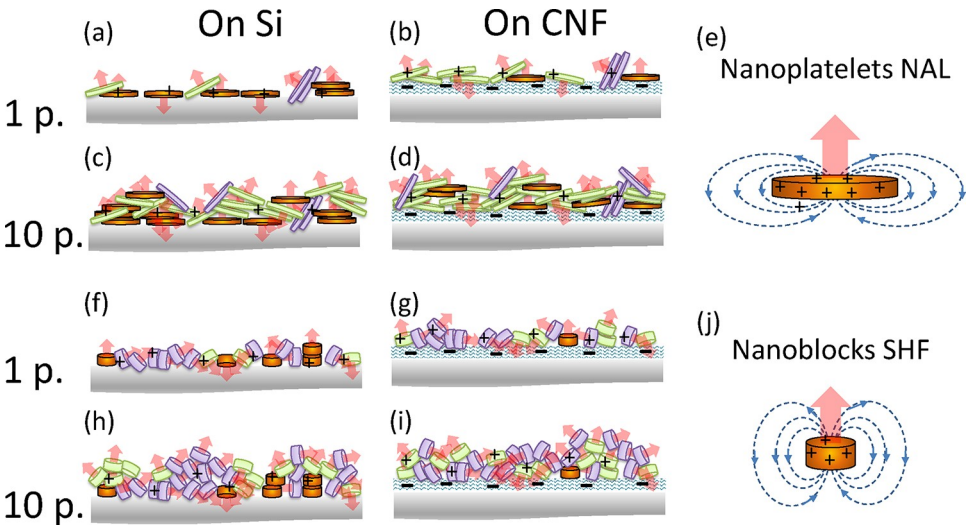

Figure 6. Model of deposited MNPs after 1 (a, b, f, g) and 10 (c, d, h, i) spray pulses of nanoplatelets NAL (a−d) and nanoblocks SHF (f−i) on the Si (a, c, f, h) or cellulose CNF (b, d, g, i) substrate. Red semitransparent arrays demonstrate the orientation of the magnetocrystalline magnetic moment of nanoparticles together with the remagnetization fields, shown by a blue dashed line with array (e, j). "+" and "−" show the presence of the positive surface charge on the surface of MNPs in the liquid medium (a−j) and negative surface charge of the CNF substrate (b, d, g, i), respectively. Brown, green, and purple colors of nanoparticles correspond to the parallel (par), near the parallel (near_par), and nonparallel (other) planes of nanoparticles, respectively, and correspond to the colors in Figure 4 and described in the main text.

https://doi.org/10.1021/acsanm.1c04568
ACS Appl. Nano Mater. 2022, 5, 8741−8754

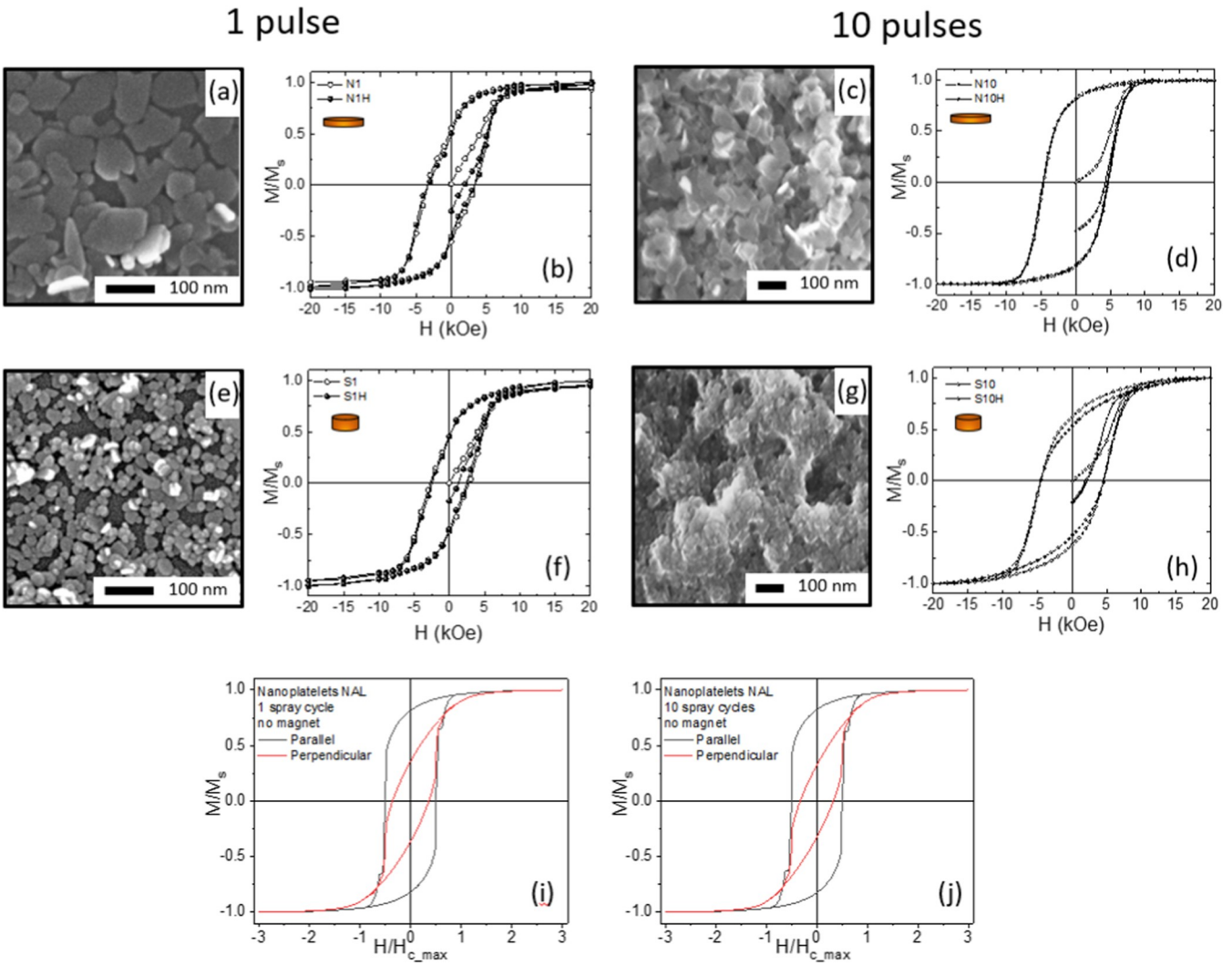

Figure 7. SEM images (a, c, e, g) and normalized $M/M_s(H)$ SQUID hysteresis loops (b, d, f, h) of the samples based on nanoplates (a–d) and nanoblocks (e–h) on silicon wafer without and under the external magnetic field B during the sample preparation after 1 (a, b, e, f) and 10 (c, d, g, h) spray pulses of ferromagnetic colloids. Theoretical remagnetization curves for oriented platelet ensembles obtained according to the Stoner–Wohlfarth model of noninteracting magnetic particles. Orientational distributions were taken from the WAXS azimuthal integration for 1 (i) and 10 (j) spray pulses.

radius and distance of the MNPs and their agglomerates. Two kinds of main parameters were varied: radius (r_1, r_2, R_3) and distance (D_1, D_2, D_3). The smallest length scales r_1 and D_1 correspond to the thickness and distance of some stuck, vertically oriented nanoparticles, r_2 and D_2—radius of the horizontal nanoparticles and distance between the neighboring ones, R_3 and D_3—radius and distance of agglomerations of nanoparticles (see the Supporting Information, Table S3 and Figure S13). Examples of the GISAXS fit of the samples S10 and S1 after 10 and 1 spray pulses of nanoblocks SHF on the Si substrate are shown in the Supporting Information, Figure S14.

The results of all of the fittings are presented in Figure 5. The thickness and distance of the stack of vertically and horizontally oriented nanoparticles r_1, r_2 (Figure 5a,c) and D_1, D_2 (Figure 5b,d) mainly correspond to the MNPs' size (height, radius) and distances in the vertical stacking and horizontal (in-plane) direction. D_1 and D_2 yield the closest distance for both kinds of nanoparticles. The minimal radii and distances of agglomerations of nanoplatelets NAL R_3 and D_3 have larger sizes after 1 pulse than after 10 pulses and demonstrate a slight increase in the presence of the external magnetic field. A larger size of agglomerates is observed at the initial moment of the formation of a film based on the CNF template. With the increasing number of spray pulses, the agglomerates' size decreases in comparison with the samples on a silicon substrate. This is comparable to our previous finding.[46] The nanoporous CNF template reduces the coffee ring effect and leads to a more homogeneous spatial distribution of the MNP. For the case of nanoblocks SHF, on the contrary, the average size of agglomerates on the CNF template is slightly smaller than for the silicon substrate, which also shows a decreasing behavior with increasing film thickness. This is due to the limited migration of MNPs with different aspect ratios of nanoblocks and nanoplatelets during the drying of the colloid under conditions of noncharged or oppositely charged substrate. The effect of an external magnetic field leads to the enlargement of agglomerates of nanoblocks SHF. This enlargement of agglomerates in an external magnetic field occurs as a consequence of the reorientation of particles having hard-magnetic moments during the drying process. There is a strong demagnetizing field around each MNP (Figure 6e,j). Neighboring particles with a parallel, unidirectional orientation

https://doi.org/10.1021/acsanm.1c04568
ACS Appl. Nano Mater. 2022, 5, 8741–8754

of magnetic moments will be repelled by their demagnetizing fields more than in a denser packing with oppositely directed neighboring moments in the absence of an external field. This will lead to the less tight packing of neighboring MNPs. Subsequently, spray-deposited MNPs should be oriented according to the moments and demagnetizing fields of the already fixed lower layer of particles. There will be an increase in magnetic properties from unidirectional magnetic particles inside local agglomerates with an even stronger repulsive demagnetizing field. Thus, conditions will be created for the consolidation of agglomerates in the process of spraying the colloid in a magnetic field. This confirms our above-mentioned results on the parallel layering of the first deposited layer of MNPs.

The presence of void spaces between the particles is well confirmed by the volumetric magnetization of the deposited films being significantly below the previously measured saturation magnetization of $SrFe_{12}O_{19}$ nanoplatelets.[40] SQUID allows for defining the volume magnetic properties.[61] The studies of the local distribution of magnetic moments of nanoparticles have also an undoubted interest and can be performed by methods such as MFM and polarized neutron reflectometry.[62] An "ideal dense" MNP film would have a thickness as deduced from SQUID measurements around 10 nm for 1 spray pulse for NAL and SHD and around 80 nm for NAL and 130 nm for SHF after 10 spray pulses (see the Supporting Information, Table S4). The void spacing manifests itself as a difference between the recalculated thickness of the theoretical dense magnetic film of $SrFe_{12}O_{19}$ from the saturation magnetization of the studied samples (Supporting Information, Table S4) and the height of the magnetic film thickness, derived from atomic force microscopy, which is varied around 300 nm (AFM; Table S5). The average roughness R_a determined by the AFM method for samples after one spray pulse varies in the range of 17−25 nm depending on the aspect ratio and the type of MNPs (Table S5). R_a is directly related to the thickness of the particles (5−7 nm) and the possibility of their stacking in several layers. This parameter can be improved by further improvement of the deposition technology.

The magnetic properties (Supporting Information, Figure S15) of the samples reveal a big difference in the magnetic reversal behavior. Full magnetic parameters of the samples are summarized in the Supporting Information, Table S4. The first significant difference consists of very different coercive forces observed for single- and multilayered samples. H_C grows from ∼3 to ∼5 kOe with the deposition of multiple layers. This behavior neither fits the intrinsic coercive force of the MNPs of ∼4 kOe observed in the frozen colloids, which stays constant, nor does it fit the platelets' thread formation,[41] leading to the growth of the coercive force (Table S4 and Figure 7i,j). To explain a diminution of the coercive force in thin layers compared to the intrinsic coercive force of MNPs, we suggest that their magnetic properties can be seriously affected by the second layer configuration (Figure S1a). The second layer allows for a reduction of the coercive force with pyramidal stacking. In such a case, a collective demagnetizing field of the particles can give rise to facilitated templating at the overlaid MNP edges and easier magnetic reversal, as has been confirmed by micromagnetic simulations (Figure S1). In the case of stacked columns of the particles (one over another), the simulations result in coercive force enhancement to ∼5 kOe (Figures S1b and 7i,j). The same effect is observed for thick platelet (NAL) layers. Thus, the collective effects of stacked particles in the thin layers (1 pulse) are considered to result in a substantial variation of the films' magnetic behavior due to the packing-dependent coupling of demagnetizing fields. The shape of the remagnetization curve is influenced by the hexaferrite nanoparticle position and number in the stacks. A huge drop in the coercive field due to the particle magnetic interaction is observed in modeling (Supporting Information, Figure S1a).

The difference between single-pulse and 10-pulse coating remagnetization curves can be attributed to particle packing and orientation on the substrate. The SEM imaging reveals that the particles in the first layer tend to orient their surface parallel to the substrate (Figures 7a,e, S3, and S16a,e). The following layers inherit this preferential orientation (Figure 7c,g). Due to hexaferrite uniaxial magnetic anisotropy (the easy axis is aligned parallel to the particle axis; Figure 6e,j), such samples will exhibit a highly anisotropic magnetic response. However, the hysteresis curve and remnant to the saturation magnetization ratio (M_r/M_s) depend on particle mutual arrangement (Figure 7b,d,f,h). Micromagnetic modeling of the remagnetization process was performed to determine the influence of the most probable layouts (Figures 7i,j and S1). The resulting values are consistent with the magnetizing/demagnetizing particle field influence. In the case of particles stacked alongside their axis, the overall field effect can be described as a magnetizing, increasing coercive field value, even for two particles (Figure S1b). The nearby particle location in the same layer induces nearly negligible fields on particles with a minimal effect on the overall coercivity. The most interesting effect is induced by shifted stacks of particles (Figure S1a). The resulting remagnetization curves show a considerably lower coercive force due to a high unobvious demagnetizing field applied in such a configuration. The described effects correspond well with experimental hysteresis curves where single-pulse coating exhibits lower coercivity values than thick films or even dried particle powder.

The increase of the coercive force with the decreasing distance of the MNPs according to the modeling estimations in the Supporting Information, Figure S1b, is also accompanied by an increased M_r/M_s ratio (see the Supporting Information, Figure S15), reflecting perpendicular anisotropy of the media. In the case of the thick nanoplatelet NAL films, the squareness of magnetic hysteresis reaches 88%, which corresponds with the predominant packing in the bulk of particles parallel to the plane of the substrate, as detected by GIWAXS. On the other hand, the films deposited onto CNF substrates expose less pronounced anisotropy, retaining M_r/M_s up to 80% (see Table S4 and Figure S16d,h). The films built from nanoblock SHF dispersions exhibit a much less preferential orientation parallel to the substrate, compared with nanoplatelets, and the magnetic hysteresis squareness ratio is <60% for both Si and CNF templates. It coincides very well with the modeled computed coercive force dependence of nanoblock stacks in the film plane (Supporting Information, Figure S1b) and might be assigned to the domination of magnetic stacked interparticle interactions over the interparticle interaction between the horizontally distributed MNPs along the substrate. Notably, the layer-by-layer deposition in the presence of an external magnetic field does not induce considerable order nor influences the perpendicular anisotropy of thicker films. This suggests the importance of interparticle stacking. On the other hand, deposition in the presence of an external magnetic field

https://doi.org/10.1021/acsanm.1c04568
ACS Appl. Nano Mater. 2022, 5, 8741−8754

always provides high enough residual magnetization M_{r0}, reaching ~0.6M_s in the case of large nanoplatelets (see Figures 7d, S15, and S16d). Thus, the development of the perpendicular anisotropy media requires deliberate attention to be paid to magnetic interactions and particle stacking options.

MNP FILM FORMATION MODEL

Combining the above data from the different, complementary measurements, we can finally deduce the following model for patterned MNP film formation from the spray-deposited colloids of hard-magnetic nanoplatelets of $SrFe_{12}O_{19}$ (Figure 6). On the first deposition cycle, the MNPs stick to the surface of the substrate due to the initial shape anisotropy and existing charge interactions (Figure 6a,b,f,g). The higher the anisotropy/aspect ratio of the MNPs, the easier they align along the surface plane. The nanoplatelet orientations are rather not influenced by an external magnetic field (Figure 6a,b). At this stage, a close-to-monolayer coverage of the substrate is achievable with a proper choice of platelet size, anisotropy, and concentration in the colloid. A second-layer configuration significantly affects the magnetic properties of thin (1−2 layer) films, giving rise to the packing-dependent coupling of demagnetizing fields. They are depicted in Figure 6e.

In the following deposition cycles, the orientation of deposited nanoparticles is influenced by the superposition of the strong magnetic field of the underlying layer and the surface relief. The nanoparticles with higher shape anisotropy (nanoplatelets, NAL) and dominantly stacking parallel to the substrate plane retain the perpendicular magnetic anisotropy of the medium (Figure 6c,d). Smaller-aspect-ratio particles (SHF, nanoblocks, Figure 7f−i) are more subjected to reorientation under the effect of the local magnetic fields from previously deposited layers due to the lower aspect ratio (2.5). The small aspect ratio allows an easier change of orientation in liquid media[63] and occupies a suitable deep pore position. The external magnetic field of around 0.1 T, valued below the local fields of the surrounding nanoparticles, which is around 0.4 T close to the particle plane (at the distances in the order of particle diameter), does not affect the final packing, providing an effect only for the first deposited layer. This first layer acts as a templating layer for subsequent deposited MNPs. In thick films, this can lead to the in-plane ordering of threads and photonic-crystal behavior (Supporting Information, Figure S17).

CONCLUSIONS

Surfactant-free water-based colloids of hard-magnetic $SrFe_{12}O_{19}$ nanoplatelets in a combination with spray deposition and the application of an oriented external magnetic field were used to obtain ferromagnetic films with preferred orientation. GIWAXS and GISAXS, imaging and optical methods, and SQUID magnetometry were utilized to extract the distribution and orientation of the nanoparticles in the film. By choosing the type and charge of the substrate (Si or CNF nanofilm with surface charge densities of 1360 μmol/g) and the presence of the external magnetic field, it is possible to influence the position and packing of nanoparticles into the stable film by magnetic coating. A coating with a zero-compensated magnetic moment is formed without an external magnetic field due to the anisotropic nature of MNPs and their free orientation in liquid media before drying. In contrast, an external magnetic field perpendicular to the substrate leads to the formation of an anisotropic film structure patterned with remnant magnetization. In addition, the neutral hard surface of silicon promotes the predominant parallel stacking of the first layers of nanoparticles. A negatively charged, soft surface of CNF leads to a more isotropic distribution of the positively charged MNPs in the film. The use of flat particles (i.e., high diameter-to-thickness ratio) leads to their preferential stacking parallel to the surface, forming a more homogeneous film with the presence of remnant magnetization when using an external magnetic field. Reducing the MNPs' aspect ratio allows the formation of a semblance of an opal-like structure under the action of an external magnetic field. The fabricated films possess a huge perpendicular anisotropy and coercivity at very small grain sizes of <50 nm. With a facile spray deposition technique, the applicability of the proposed method to CNF films opens a pathway for flexible magnetic coatings. Thus, we can conclude that the use of the easily scalable spray method in the ambient atmosphere for the deposition of an aqueous solution of MNPs based on strontium hexaferrite makes it possible to create layers of magnetic nanoparticles. The parameters of our first obtained samples based on an aqueous solution of strontium hexaferrite nanoparticles are rather close to the best practical samples obtained for magnetic recording devices from IBM.[8] We believe that a further more detailed study of various varied technological parameters of deposition can significantly improve the structural and magnetic properties of the studied films of MNPs.

ASSOCIATED CONTENT

Supporting Information

The Supporting Information is available free of charge at https://pubs.acs.org/doi/10.1021/acsanm.1c04568.

Figures showing the modeled remagnetization curves for particle stacks; TGA analysis weight fraction of the magnetic phase in dispersion; table of the sample labeling; SEM images of the samples; GIWAXS 2D data and GIWAXS azimuthal intensity distribution of the peaks; table with the results of GIWAXS fits of the azimuthal intensity distribution; photo images of the sprayed nanoblocks on the CNF nanofilm; 2D GISAXS data of the MNPs and their off-center vertical and horizontal line-cuts; list of the parameters in the GISAXS fit; schematic representation of the GISAXS fit model; examples of the GISAXS fit; SQUID magnetization curves for the samples; table with the sample size parameters and the results of SQUID data processing; table with the results of surface structure parameters after analysis of AFM data; and the results of DC magneto-optical measurements and SAXS data from sprayed colloid (PDF)

AUTHOR INFORMATION

Corresponding Authors

Andrei Chumakov − *Deutsches Elektronen-Synchrotron DESY, 22607 Hamburg, Germany;* orcid.org/0000-0003-3195-9356; Email: andrei.chumakov@desy.de

Stephan V. Roth − *Deutsches Elektronen-Synchrotron DESY, 22607 Hamburg, Germany; Department of Fibre and Polymer Technology, KTH Royal Institute of Technology, 100 44 Stockholm, Sweden;* orcid.org/0000-0002-6940-6012; Email: stephan.roth@desy.de

https://doi.org/10.1021/acsanm.1c04568
ACS Appl. Nano Mater. 2022, 5, 8741−8754

Authors

Calvin J. Brett − *Deutsches Elektronen-Synchrotron DESY, 22607 Hamburg, Germany; Department of Fibre and Polymer Technology, KTH Royal Institute of Technology, 100 44 Stockholm, Sweden;* orcid.org/0000-0001-5789-6299

Korneliya Gordeyeva − *Department of Fibre and Polymer Technology, KTH Royal Institute of Technology, 100 44 Stockholm, Sweden*

Dirk Menzel − *Institut für Physik der Kondensierten Materie, Technische Universität Braunschweig, 38106 Braunschweig, Germany*

Lewis O. O. Akinsinde − *Institute for Nanostructures and Solid-State Physics, Center for Free-Electron Laser Science (CFEL), Universität Hamburg, 22761 Hamburg, Germany; Institute for Materials Science, Kiel University, 24143 Kiel, Germany;* orcid.org/0000-0002-2147-4542

Marc Gensch − *Deutsches Elektronen-Synchrotron DESY, 22607 Hamburg, Germany;* orcid.org/0000-0001-5514-8158

Matthias Schwartzkopf − *Deutsches Elektronen-Synchrotron DESY, 22607 Hamburg, Germany;* orcid.org/0000-0002-2115-9286

Wei Cao − *Lehrstuhl für Funktionelle Materialien, Physik Department, Technische Universität München, 85748 Garching, Germany;* orcid.org/0000-0001-7578-0900

Shanshan Yin − *Lehrstuhl für Funktionelle Materialien, Physik Department, Technische Universität München, 85748 Garching, Germany;* orcid.org/0000-0002-5363-0837

Manuel A. Reus − *Lehrstuhl für Funktionelle Materialien, Physik Department, Technische Universität München, 85748 Garching, Germany;* orcid.org/0000-0003-0508-6694

Michael A. Rübhausen − *Institute for Nanostructures and Solid-State Physics, Center for Free-Electron Laser Science (CFEL), Universität Hamburg, 22761 Hamburg, Germany*

Peter Müller-Buschbaum − *Lehrstuhl für Funktionelle Materialien, Physik Department, Technische Universität München, 85748 Garching, Germany; Heinz Maier-Leibnitz Zentrum (MLZ), Technische Universität München, 85748 Garching, Germany;* orcid.org/0000-0002-9566-6088

L. Daniel Söderberg − *Department of Fibre and Polymer Technology, KTH Royal Institute of Technology, 100 44 Stockholm, Sweden;* orcid.org/0000-0003-3737-0091

Complete contact information is available at: https://pubs.acs.org/10.1021/acsanm.1c04568

Author Contributions

The manuscript was written with contributions from all authors.

Notes

The authors declare no competing financial interest.

■ ACKNOWLEDGMENTS

The authors thank the synchrotron light source PETRA III and the beamline P03 at Deutsches Elektronen-Synchrotron DESY for beam time allocation. C.J.B. and S.V.R. acknowledge funding via the DESY strategic fund (DSF) under grant number "Investigation of processes for spraying and spray coating of hybrid cellulose-based nanostructures"/DSF-16. W.C. and S.Y. acknowledge the China Scholarship Council (CSC). DESY is a member of the Helmholtz Association (HGF). The authors thank Andrei A. Eliseev, Artem A. Eliseev, Evgeny O. Anokhin, and Lev A. Trusov for proving the MNP synthesis, magnetic simulations, and TEM measurements.

■ REFERENCES

(1) Zhang, M.; Wang, M.; Zhang, M.; Maimaitiming, A.; Pang, L.; Liang, Y.; Hu, J.; Wu, G. Fe3O4 Nanowire Arrays on Flexible Polypropylene Substrates for UV and Magnetic Sensing. *ACS Appl. Nano Mater.* **2018**, *1*, 5742−5752.

(2) Mittal, N.; Ansari, F.; Gowda Krishne, V.; Brouzet, C.; Chen, P.; Larsson, P. T.; Roth, S. V.; Lundell, F.; Wågberg, L.; Kotov, N. A.; Söderberg, L. D. Multiscale Control of Nanocellulose Assembly: Transferring Remarkable Nanoscale Fibril Mechanics to Macroscale Fibers. *ACS Nano* **2018**, *12*, 6378−6388.

(3) Niemelä, J.-P.; Philip, A.; Rohbeck, N.; Karppinen, M.; Michler, J.; Utke, I. Mechanics of Nanoscale ϵ-Fe2O3/Organic Superlattices toward Flexible Thin-Film Magnets. *ACS Appl. Nano Mater.* **2021**, *4*, 1692−1701.

(4) Sheng, P.; Wang, B.; Li, R. Flexible Magnetic Thin Films and Devices. *J. Semicond.* **2018**, *39*, No. 011006.

(5) Blachowicz, T.; Ehrmann, A. Most Recent Developments in Electrospun Magnetic Nanofibers: A Review. *J. Eng. Fibers Fabrics* **2020**, *15*, No. 155892501990084.

(6) Gaspar, J.; Fonseca, H.; Paz, E.; Martins, M.; Valadeiro, J.; Cardoso, S.; Ferreira, R.; Freitas, P. P. Flexible Magnetoresistive Sensors Designed for Conformal Integration. *IEEE Trans. Magn.* **2017**, *53*, 1−4.

(7) Zheng, C.; Zhu, K.; Cardoso de Freitas, S.; Chang, J.-Y.; Davies, J. E.; Eames, P.; Freitas, P. P.; Kazakova, O.; Kim, C.; Leung, C.-W.; Liou, S.-H.; Ognev, A.; Piramanayagam, S. N.; Ripka, P.; Samardak, A.; Shin, K.-H.; Tong, S.-Y.; Tung, M.-J.; Wang, S. X.; Xue, S.; Yin, X.; Pong, P. W. T. Magnetoresistive Sensor Development Roadmap (Non-Recording Applications). *IEEE Trans. Magn.* **2019**, *55*, 1−30.

(8) Furrer, S.; Ebermann, P.; Lantz, M. A.; Rothuizen, H.; Haeberle, W.; Cherubini, G.; Cideciyan, R. D.; Tsujimoto, S.; Sawayashiki, Y.; Imaoka, N.; Murata, Y.; Ueyama, T.; Akano, Y.; Kaneko, T.; Suzuki, H.; Shirata, M.; Naoi, K.; Koike, T.; Doshita, H. 317 Gb/in 2 Recording Areal Density on Strontium Ferrite Tape. *IEEE Trans. Magn.* **2021**, *57*, 1−11.

(9) Furrer, S.; Lantz, M. A.; Reininger, P.; Pantazi, A.; Rothuizen, H. E.; Cideciyan, R. D.; Cherubini, G.; Haeberle, W.; Eleftheriou, E.; Tachibana, J.; Sekiguchi, N.; Aizawa, T.; Endo, T.; Ozaki, T.; Sai, T.; Hiratsuka, R.; Mitamura, S.; Yamaguchi, A. 201 Gb/in 2 Recording Areal Density on Sputtered Magnetic Tape. *IEEE Trans. Magn.* **2018**, *54*, 1−8.

(10) Shimizu, O.; Kurihashi, Y.; Watanabe, I.; Harasawa, T. Distribution of Thermal Stability Factor for Barium Ferrite Particles. *IEEE Trans. Magn.* **2013**, *49*, 3767−3770.

(11) Trusov, L. A.; Sleptsova, A. E.; Duan, J.; Gorbachev, E. A.; Kozlyakova, E. S.; Anokhin, E. O.; Eliseev, A. A.; Karpov, M. A.; Vasiliev, A. V.; Brylev, O. A.; Kazin, P. E. Glass-Ceramic Synthesis of Cr-Substituted Strontium Hexaferrite Nanoparticles with Enhanced Coercivity. *Nanomaterials* **2021**, *11*, 924.

(12) Alahmed, L.; Li, P. Perpendicular Magnetic Insulator Films for Spintronics. In *Magnetic Materials and Magnetic Levitation*, Sahu, D. R.; Stavrou, V. N., Eds.; IntechOpen, 2021.

(13) Zhao, S.; Zhou, Z.; Li, C.; Peng, B.; Hu, Z.; Liu, M. Low-Voltage Control of (Co/Pt) x Perpendicular Magnetic Anisotropy Heterostructure for Flexible Spintronics. *ACS Nano* **2018**, *12*, 7167−7173.

(14) Vemulkar, T.; Mansell, R.; Fernández-Pacheco, A.; Cowburn, R. P. Toward Flexible Spintronics: Perpendicularly Magnetized Synthetic Antiferromagnetic Thin Films and Nanowires on Polyimide Substrates. *Adv. Funct. Mater.* **2016**, *26*, 4704−4711.

(15) Quindeau, A.; Avci, C. O.; Liu, W.; Sun, C.; Mann, M.; Tang, A. S.; Onbasli, M. C.; Bono, D.; Voyles, P. M.; Xu, Y.; Robinson, J.; Beach, G. S. D.; Ross, C. A. Tm3Fe5O12/Pt Heterostructures with Perpendicular Magnetic Anisotropy for Spintronic Applications. *Adv. Electron. Mater.* **2017**, *3*, No. 1600376.

(16) Zhou, L.; Mao, J.; Ren, Y.; Han, S. T.; Roy, V. A. L.; Zhou, Y. Recent Advances of Flexible Data Storage Devices Based on Organic Nanoscaled Materials. *Small* **2018**, *14*, No. 1703126.
(17) Heijnen, S. M. F.; van Vliet, P.; Kuipers, B. W. M.; Philipse, A. P.; Petukhov, A. V.; Ouhajji, S. Depletion-Induced Chiral Chain Formation of Magnetic Spheres. *Materials* **2021**, *14*, No. 507.
(18) Rahmatika, A. M.; Toyoda, Y.; Nguyen, T. T.; Goi, Y.; Kitamura, T.; Morita, Y.; Kume, K.; Ogi, T. Cellulose Nanofiber and Magnetic Nanoparticles as Building Blocks Constructing Biomass-Based Porous Structured Particles and Their Protein Adsorption Performance. *ACS Sustainable Chem. Eng.* **2020**, *8*, 18686−18695.
(19) Wang, Y.; Chen, X.; Zhang, Z.; Li, T.; Zhang, X.; Xia, B.; Chen, M.; Liu, T.; Dong, W. Fe3O4Nanoparticle-Decorated Graphene Oxide Nanosheets for Magnetic Assembly of Artificial Nacre. *ACS Appl. Nano Mater.* **2021**, *4*, 9689−9696.
(20) Sarathlal, K. V.; Kumar, D.; Gupta, A. Growth Study of Co Thin Film on Nanorippled Si(100) Substrate. *Appl. Phys. Lett.* **2011**, *98*, No. 123111.
(21) Theis-Bröhl, K.; Gutfreund, P.; Vorobiev, A.; Wolff, M.; Toperverg, B. P.; Dura, J. A.; Borchers, J. A. Self Assembly of Magnetic Nanoparticles at Silicon Surfaces. *Soft Matter* **2015**, *11*, 4695−4704.
(22) Ngoi, K. H.; Wong, J. C.; Chiu, W. S.; Chia, C. H.; Jin, K. S.; Kim, H.-J.; Kim, H.-C.; Ree, M. Morphological Structure Details, Size Distributions and Magnetic Properties of Iron Oxide Nanoparticles. *J. Ind. Eng. Chem.* **2021**, *95*, 37−50.
(23) Masoudpanah, S. M.; Seyyed Ebrahimi, S. A.; Ong, C. K. Magnetic Properties of Strontium Hexaferrite Films Prepared by Pulsed Laser Deposition. *J. Magn. Magn. Mater.* **2012**, *324*, 2654−2658.
(24) Saura-Múzquiz, M.; Granados-Miralles, C.; Andersen, H. L.; Stingaciu, M.; Avdeev, M.; Christensen, M. Nanoengineered High-Performance Hexaferrite Magnets by Morphology-Induced Alignment of Tailored Nanoplatelets. *ACS Appl. Nano Mater.* **2018**, *1*, 6938−6949.
(25) Schwartzkopf, M.; Hinz, A.; Polonskyi, O.; Strunskus, T.; Löhrer, F. C.; Körstgens, V.; Müller-Buschbaum, P.; Faupel, F.; Roth, S. V. Role of Sputter Deposition Rate in Tailoring Nanogranular Gold Structures on Polymer Surfaces. *ACS Appl. Mater. Interfaces* **2017**, *9*, 5629−5637.
(26) Roth, S. V.; Santoro, G.; Risch, J. F. H.; Yu, S.; Schwartzkopf, M.; Boese, T.; Döhrmann, R.; Zhang, P.; Besner, B.; Bremer, P.; Rukser, D.; Rübhausen, M. A.; Terrill, N. J.; Staniec, P. A.; Yao, Y.; Metwalli, E.; Müller-Buschbaum, P. Patterned Diblock Co-Polymer Thin Films as Templates for Advanced Anisotropic Metal Nanostructures. *ACS Appl. Mater. Interfaces* **2015**, *7*, 12470−12477.
(27) Erb, D. J.; Schlage, K.; Röhlsberger, R. Uniform Metal Nanostructures with Long-Range Order via Three-Step Hierarchical Self-Assembly. *Sci. Adv.* **2015**, *1*, No. 1500751.
(28) Céspedes, E.; Rodriguez-Rodriguez, G.; Navío, C.; Osorio, M. R.; Guerrero, R.; Pedrosa, F. J.; Mompeán, F. J.; García-Hernández, M.; Fernández, J. F.; Quesada, A.; Camarero, J.; Bollero, A. Inter-Grain Effects on the Magnetism of M-Type Strontium Ferrite. *J. Alloys Compd.* **2017**, *692*, 280−287.
(29) Deng, K.; Luo, Z.; Tan, L.; Quan, Z. Self-Assembly of Anisotropic Nanoparticles into Functional Superstructures. *Chem. Soc. Rev.* **2020**, *49*, 6002−6038.
(30) Roth, S. V. A Deep Look into the Spray Coating Process in Real-Time—the Crucial Role of x-Rays. *J. Phys.: Condens. Matter* **2016**, *28*, No. 403003.
(31) Zhang, P.; Reiser, B.; González-García, L.; Beck, S.; Drzic, J.; Kraus, T. Drying of Electrically Conductive Hybrid Polymer−Gold Nanorods Studied with in Situ Microbeam GISAXS. *Nanoscale* **2019**, *11*, 6538−6543.
(32) Smith, A. T.; LaChance, A. M.; Zeng, S.; Liu, B.; Sun, L. Synthesis, Properties, and Applications of Graphene Oxide/Reduced Graphene Oxide and Their Nanocomposites. *Nano Mater. Sci.* **2019**, *1*, 31−47.
(33) Chernova, E. A.; Petukhov, D. I.; Chumakov, A. P.; Kirianova, A. V.; Sadilov, I. S.; Kapitanova, O. O.; Boytsova, O. V.; Valeev, R. G.; Roth, S. V.; Eliseev, A. A.; Eliseev, A. A. The Role of Oxidation Level in Mass-Transport Properties and Dehumidification Performance of Graphene Oxide Membranes. *Carbon* **2021**, *183*, 404−414.
(34) Petukhov, D. I.; Chumakov, A. P.; Kan, A. S.; Lebedev, V. A.; Eliseev, A. A.; Konovalov, O. V.; Eliseev, A. A. Spontaneous MXene Monolayer Assembly at the Liquid−Air Interface. *Nanoscale* **2019**, *11*, 9980−9986.
(35) Shimizu, O.; Oyanagi, M.; Morooka, A.; Mori, M.; Kurihashi, Y.; Tada, T.; Suzuki, H.; Harasawa, T. Development of Advanced Barium Ferrite Tape Media. *J. Magn. Magn. Mater.* **2016**, *400*, 365−369.
(36) Anokhin, E. O.; Trusov, L. A.; Kozlov, D. A.; Chumakov, R. G.; Sleptsova, A. E.; Uvarov, O. V.; Kozlov, M. I.; Petukhov, D. I.; Eliseev, A. A.; Kazin, P. E. Silica Coated Hard-Magnetic Strontium Hexaferrite Nanoparticles. *Adv. Powder Technol.* **2019**, *30*, 1976−1984.
(37) Trusov, L. A.; Babarkina, O. V.; Anokhin, E. O.; Sleptsova, A. E.; Gorbachev, E. A.; Eliseev, A. A.; Filippova, T. V.; Vasiliev, A. V.; Kazin, P. E. Crystallization of Magnetic Particles in NNa2O-9SrO-6Fe2O3-8B2O3 (n = 1 and 4) Glasses. *J. Magn. Magn. Mater.* **2019**, *476*, 311−316.
(38) Trusov, L. A.; Vasiliev, A. V.; Lukatskaya, M. R.; Zaytsev, D. D.; Jansen, M.; Kazin, P. E. Stable Colloidal Solutions of Strontium Hexaferrite Hard Magnetic Nanoparticles. *Chem. Commun.* **2014**, *50*, 14581−14584.
(39) Shirk, B. T.; Buessem, W. R. Temperature Dependence of M s and K 1 of BaFe 12 O 19 and SrFe 12 O 19 Single Crystals. *J. Appl. Phys.* **1969**, *40*, 1294−1296.
(40) Eliseev, A. A.; Eliseev, A. A.; Trusov, L. A.; Chumakov, A. P.; Boesecke, P.; Anokhin, E. O.; Vasiliev, A. V.; Sleptsova, A. E.; Gorbachev, E. A.; Korolev, V. V.; Kazin, P. E. Rotational Dynamics of Colloidal Hexaferrite Nanoplates. *Appl. Phys. Lett.* **2018**, *113*, No. 113106.
(41) Eliseev, A. A.; Trusov, L. A.; Anokhin, E. O.; Chumakov, A. P.; Korolev, V. V.; Sleptsova, A. E.; Boesecke, P.; Pryakhina, V. I.; Shur, V. Y.; Kazin, P. E.; Eliseev, A. A. Tunable Order in Colloids of Hard Magnetic Hexaferrite Nanoplatelets. *Nano Res.* **2022**, *15*, 898−906.
(42) Cao, W.; Yin, S.; Plank, M.; Chumakov, A.; Opel, M.; Chen, W.; Kreuzer, L. P.; Heger, J. E.; Gallei, M.; Brett, C. J.; Schwartzkopf, M.; Eliseev, A. A.; Anokhin, E. O.; Trusov, L. A.; Roth, S. V.; Müller-Buschbaum, P. Spray-Deposited Anisotropic Ferromagnetic Hybrid Polymer Films of PS- b -PMMA and Strontium Hexaferrite Magnetic Nanoplatelets. *ACS Appl. Mater. Interfaces* **2021**, *13*, 1592−1602.
(43) Xia, S.; Song, L.; Hohn, N.; Wang, K.; Grott, S.; Opel, M.; Schwartzkopf, M.; Roth, S. V.; Müller-Buschbaum, P. Spray-Coating Magnetic Thin Hybrid Films of PS- b -PNIPAM and Magnetite Nanoparticles. *Adv. Funct. Mater.* **2019**, *29*, No. 1808427.
(44) Lisjak, D.; Bobzin, K.; Richardt, K.; Bégard, M.; Bolelli, G.; Lusvarghi, L.; Hujanen, A.; Lintunen, P.; Pasquale, M.; Olivetti, E.; Drofenik, M.; Schläfer, T. Preparation of Barium Hexaferrite Coatings Using Atmospheric Plasma Spraying. *J. Eur. Ceram. Soc.* **2009**, *29*, 2333−2341.
(45) Johnson, S. D.; Schwer, D.; Park, D.-S.; Park, Y.-S.; Gorzkowski, E. P. Deposition Efficiency of Barium Hexaferrite by Aerosol Deposition. *Surf. Coat. Technol.* **2017**, *332*, 542−549.
(46) Chen, Q.; Brett, C. J.; Chumakov, A.; Gensch, M.; Schwartzkopf, M.; Körstgens, V.; Söderberg, L. D.; Plech, A.; Zhang, P.; Müller-Buschbaum, P.; Roth, S. V. Layer-by-Layer Spray-Coating of Cellulose Nanofibrils and Silver Nanoparticles for Hydrophilic Interfaces. *ACS Appl. Nano Mater.* **2021**, *4*, 503−513.
(47) Mao, Y.; Liu, K.; Zhan, C.; Geng, L.; Chu, B.; Hsiao, B. S. Characterization of Nanocellulose Using Small-Angle Neutron, X-Ray, and Dynamic Light Scattering Techniques. *J. Phys. Chem. B* **2017**, *121*, 1340−1351.
(48) Brett, C. J.; Mittal, N.; Ohm, W.; Gensch, M.; Kreuzer, L. P.; Körstgens, V.; Månsson, M.; Frielinghaus, H.; Müller-Buschbaum, P.; Söderberg, L. D.; Roth, S. V. Water-Induced Structural Rearrange-

https://doi.org/10.1021/acsanm.1c04568
ACS Appl. Nano Mater. 2022, 5, 8741−8754

ments on the Nanoscale in Ultrathin Nanocellulose Films. *Macromolecules* **2019**, *52*, 4721−4728.
(49) Benítez, A. J.; Walther, A. Cellulose Nanofibril Nanopapers and Bioinspired Nanocomposites: A Review to Understand the Mechanical Property Space. *J. Mater. Chem. A* **2017**, *5*, 16003−16024.
(50) Zhang, P.; Santoro, G.; Yu, S.; Vayalil, S. K.; Bommel, S.; Roth, S. V. Manipulating the Assembly of Spray-Deposited Nanocolloids: In Situ Study and Monolayer Film Preparation. *Langmuir* **2016**, *32*, 4251−4258.
(51) Zi, Z. F.; Sun, Y. P.; Zhu, X. B.; Yang, Z. R.; Dai, J. M.; Song, W. H. Structural and Magnetic Properties of SrFe12O19 Hexaferrite Synthesized by a Modified Chemical Co-Precipitation Method. *J. Magn. Magn. Mater.* **2008**, *320*, 2746−2751.
(52) Nečas, D.; Klapetek, P. Gwyddion: An Open-Source Software for SPM Data Analysis. *Open Phys.* **2012**, *10*, 181−188.
(53) Buffet, A.; Rothkirch, A.; Döhrmann, R.; Körstgens, V.; Abul Kashem, M. M.; Perlich, J.; Herzog, G.; Schwartzkopf, M.; Gehrke, R.; Müller-Buschbaum, P.; Roth, S. V. P03, the Microfocus and Nanofocus X-Ray Scattering (MiNaXS) Beamline of the PETRA III Storage Ring: The Microfocus Endstation. *J. Synchrotron Radiat.* **2012**, *19*, 647−653.
(54) Donahue, M. J.; Porter, D. G. *OOMMF User's Guide*, version 1.0, National Institute of Standards and Technology, 1999.
(55) Kazin, P. E.; Trusov, L. A.; Zaitsev, D. D.; Tretyakov, Y. D.; Jansen, M. Formation of Submicron-Sized SrFe12−xAlxO19 with Very High Coercivity. *J. Magn. Magn. Mater.* **2008**, *320*, 1068−1072.
(56) Kazin, P. E.; Trusov, L. A.; Zaitsev, D. D.; Tret'Yakov, Y. D. Glass Crystallization Synthesis of Ultrafine Hexagonal M-Type Ferrites: Particle Morphology and Magnetic Characteristics. *Russ. J. Inorg. Chem.* **2009**, *54*, 2081−2090.
(57) Peddis, D.; Jönsson, P. E.; Laureti, S.; Varvaro, G. Magnetic Interactions. *Front. Nanosci.* **2014**, *6*, 129−188.
(58) Zhang, P.; Rothkirch, A.; Koch, M.; Roth, S.; Kraus, T. Determination of the Surface Facets of Gold Nanorods in Wet-Coated Thin Films with Grazing-Incidence Wide Angle X-Ray Scattering. *Part. Part. Syst. Charact.* **2019**, *36*, No. 1900323.
(59) Hexemer, A.; Müller-Buschbaum, P. Advanced Grazing-Incidence Techniques for Modern Soft-Matter Materials Analysis. *IUCrJ* **2015**, *2*, 106−125.
(60) Schwartzkopf, M.; Roth, S. V. Investigating Polymer-Metal Interfaces by Grazing Incidence Small-Angle X-Ray Scattering from Gradients to Real-Time Studies. *Nanomaterials* **2016**, *6*, 239.
(61) Liscio, F.; Makarov, D.; Maret, M.; Doisneau-Cottignies, B.; Roussel, H.; Albrecht, M. Growth, Structure and Magnetic Properties of FePt Nanostructures on NaCl(001) and MgO(001). *Nanotechnology* **2010**, *21*, No. 065602.
(62) Zabel, H.; Theis Brohl, K.; Wolff, M.; Toperverg, B. P. Polarized Neutron Reflectometry for the Analysis of Nanomagnetic Systems. *IEEE Trans. Magn.* **2008**, *44*, 1928−1934.
(63) Rosén, T.; Wang, R.; Zhan, C.; He, H.; Chodankar, S.; Hsiao, B. S. Cellulose Nanofibrils and Nanocrystals in Confined Flow: Single-Particle Dynamics to Collective Alignment Revealed through Scanning Small-Angle x-Ray Scattering and Numerical Simulations. *Phys. Rev. E* **2020**, *101*, No. 032610.

https://doi.org/10.1021/acsanm.1c04568
ACS Appl. Nano Mater. 2022, 5, 8741−8754